

Article

# Synthesis of $\text{Ag}_3\text{PO}_4/\text{g-C}_3\text{N}_4$ Composite with Enhanced Photocatalytic Performance for the Photodegradation of Diclofenac under Visible Light Irradiation

Wei Zhang, Li Zhou, Jun Shi \* and Huiping Deng \*

State Key Laboratory of Pollution Control and Resource Reuse, College of Environmental Science and Engineering, Tongji University, Shanghai 200092, China; 1310401@tongji.edu.cn (W.Z.); joly.zhoul@gmail.com (L.Z.)

\* Correspondence: shijun215@tongji.edu.cn (J.S.); 13567@tongji.edu.cn (H.D.); Tel.: +86-021-6598-1510 (J.S.)

Received: 3 December 2017; Accepted: 23 January 2018; Published: 25 January 2018

**Abstract:** A new visible-light-driven heterojunction  $\text{Ag}_3\text{PO}_4/\text{g-C}_3\text{N}_4$  was prepared by a simple deposition-precipitation method for the degradation analysis of diclofenac (DCF), a model drug component, under visible-light irradiation. The heterojunction photocatalysts were characterized by a suite of tools. The results revealed that the introduction of  $\text{Ag}_3\text{PO}_4$  on the surface of  $\text{g-C}_3\text{N}_4$  greatly promoted its stability and light absorption performance. In addition, the effects of the heterojunction mixing ratios were studied, when the molar ratio of  $\text{Ag}_3\text{PO}_4$  to  $\text{g-C}_3\text{N}_4$  in the composite was 30%, the as-prepared photocatalyst  $\text{Ag}_3\text{PO}_4/\text{g-C}_3\text{N}_4$  (30%) possessed the best photocatalytic activity toward the photodegradation of DCF, and the optimal photocatalyst showed a DCF degradation rate of  $0.453 \text{ min}^{-1}$ , which was almost 34.8 and 6.4 times higher than those of pure  $\text{g-C}_3\text{N}_4$  ( $0.013 \text{ min}^{-1}$ ) and  $\text{Ag}_3\text{PO}_4$  ( $0.071 \text{ min}^{-1}$ ) under visible light irradiation ( $\lambda \geq 400 \text{ nm}$ ). The trapping experimental results showed that  $\text{h}^+$ ,  $\cdot\text{OH}$ , and  $\cdot\text{O}_2^-$  were the main reactive oxygen species during the photocatalytic reaction. The improved performance of the composites was induced by the high charge separation efficiency of the photogeneration electron-hole pairs as well as the surface plasmon resonance (SPR) endowed in the  $\text{Ag}^0$  nanoparticles, and ultimately enhanced the DCF photodegradation.

**Keywords:**  $\text{Ag}_3\text{PO}_4/\text{g-C}_3\text{N}_4$ ; heterojunction; visible-light photocatalysis; diclofenac

## 1. Introduction

Recently, semiconductor-based photocatalysts have attracted intense attention as they hold promising potential for the use of solar light for pollution degradation and environmental remediation [1,2]. The conventional  $\text{TiO}_2$  photocatalyst has been extensively investigated due to its great photoactivity, stability, and innocuousness [3]. However, since the band gap of  $\text{TiO}_2$  is 3.2 eV, it is only active under UV-light irradiation [4]. Therefore, the performance of  $\text{TiO}_2$  is limited due to the limited visible-light utilization.

Currently, some visible-light-driven photocatalysts have been reported, such as  $\text{g-C}_3\text{N}_4$ , Ag-based photocatalysts, as well as  $\text{Bi}_2\text{WO}_6$  [5–8]. However, it is very difficult to obtain a single-component photocatalyst with a wide light-absorption range and high charge-separation efficiency. Multi-component photocatalysts, which have more potential to be perfect photocatalysts, have received widespread attention [9,10]. As the energy levels of coupling semiconductors should be well matched, one of the basic conditions for constructing a heterojunction is to find two semiconductors with suitable band structure.

After Ye et al. first reported  $\text{Ag}_3\text{PO}_4$  with photooxidation properties under visible light irradiation in 2000 [11], more and more research demonstrated its promising photocatalytic performance in

water oxidation and organic-contaminant photodegradation. It has been reported that  $\text{Ag}_3\text{PO}_4$  can achieve a quantum efficiency of up to 90% at wavelengths greater than 420 nm, which are significantly higher than that of previously reported semiconductors [12,13]. However, due to the conduction band potential (CB) in  $\text{Ag}_3\text{PO}_4$  (+0.45 eV, vs. NHE) being more positive than the reduction potential of  $\text{O}_2/\cdot\text{O}_2^-$  (−0.33 eV, vs. NHE), the generated electrons cannot combine with the  $\text{O}_2$  to form active species for photo-oxidation during the photocatalytic process [11]. In addition,  $\text{Ag}_3\text{PO}_4$  can be easily reduced to  $\text{Ag}^0$  by the electrons generated during the photocatalytic reactions, leading to the photocorrosion of  $\text{Ag}_3\text{PO}_4$ . Furthermore,  $\text{Ag}_3\text{PO}_4$  is slightly soluble in aqueous solution, which seriously reduces its structural stability and separating efficiency in an aqueous solution [13,14]. Therefore, some strategies should be taken to enhance the photocatalytic performance and stability of  $\text{Ag}_3\text{PO}_4$ . Up until now,  $\text{Ag}_3\text{PO}_4$ -based composites synthesized by various strategies have been widely reported, such as  $\text{Ag}_3\text{PO}_4/\text{BiVO}_4$  [15],  $\text{WO}_3/\text{Ag}_3\text{PO}_4$  [16], and  $\text{Ag}_3\text{PO}_4/\text{TiO}_2$  [17]. The prepared photocatalysts have exhibited good stability and superior photocatalytic performance. Graphite carbon nitride (g- $\text{C}_3\text{N}_4$ ), a two-dimensional polymeric metal-free semiconductor, has been recently investigated in regards to water oxidation and pollution decomposition under visible light irradiation [18]. The g- $\text{C}_3\text{N}_4$  photocatalyst exhibits high thermal and chemical stability as well as novel electronic properties [19]. Furthermore, g- $\text{C}_3\text{N}_4$  presents a similar structure with graphene, which makes it a valuable candidate for combinations with other semiconductors to synthesize heterojunction composites [20,21].

As the CB and valence band (VB) positions of g- $\text{C}_3\text{N}_4$  are −1.30 and +1.40 eV (vs. NHE), and the CB and VB positions of  $\text{Ag}_3\text{PO}_4$  are +0.45 and +2.90 eV (vs. NHE) [13,22], g- $\text{C}_3\text{N}_4$  and  $\text{Ag}_3\text{PO}_4$  are two appropriate candidates for the construction of a heterostructured photocatalyst. Furthermore, the deposition of slight-soluble  $\text{Ag}_3\text{PO}_4$  on the surface of the insoluble g- $\text{C}_3\text{N}_4$  sheet can effectively protect  $\text{Ag}_3\text{PO}_4$  from dissolution due to the chemical adsorption between the g- $\text{C}_3\text{N}_4$  and  $\text{Ag}_3\text{PO}_4$ , which could enhance the structural stability of the  $\text{Ag}_3\text{PO}_4/\text{g-C}_3\text{N}_4$  composites [14,23].  $\text{Ag}_3\text{PO}_4/\text{g-C}_3\text{N}_4$  composites have shown a positive photocatalytic performance for the degradation of dyes such as methylene blue [24], rhodamine B [25], and orange methyl [26]. In addition, the composites also show an effective ability in the  $\text{CO}_2$  photoreduction process [27]. Nevertheless,  $\text{Ag}_3\text{PO}_4/\text{g-C}_3\text{N}_4$  composites are scarcely employed in the degradation of pollution materials, which are more difficult to be oxidized.

Diclofenac (DCF), a model non-steroidal anti-inflammatory drug (NSAID), is one of the most frequently detected pharmaceutical compounds in the aquatic environment [28], and its adverse impact on the current environment and ecosystems is evident. For example, DCF is toxic to fish and terrestrial vertebrates even at low concentrations [29,30]. The presence of DCF residuals in aqueous environment has also been attributed to the decline in the vulture population and the death of rainbow trout [31,32]. Traditional water treatment processes (e.g., activated carbon adsorption and coagulation) are usually insufficient for the complete removal of DCF [29–31,33,34], therefore, novel enhanced water-treatment technologies and processes are urgently needed to tackle the DCF challenges, as well as other emerging pharmaceutical pollutants in water treatment industries.

In this work, a series of  $\text{Ag}_3\text{PO}_4/\text{g-C}_3\text{N}_4$  composite photocatalysts were synthesized via a deposition-precipitation method. The DCF photodegradation under visible-light irradiation over the heterojunctions was evaluated to better understand the photocatalytic properties and activity of this novel composite catalyst. The effects of different mass ratios on photocatalytic activity were systematically compared. In addition, the stability of  $\text{Ag}_3\text{PO}_4/\text{g-C}_3\text{N}_4$  was assessed through five successive cycles. The structure, composition, morphology, and optical properties of the  $\text{Ag}_3\text{PO}_4/\text{g-C}_3\text{N}_4$  photocatalysts were also characterized and discussed. Finally, a possible mechanism for the enhanced activity of  $\text{Ag}_3\text{PO}_4/\text{g-C}_3\text{N}_4$  was discussed based on the synergetic effects of the  $\text{Ag}_3\text{PO}_4/\text{g-C}_3\text{N}_4$  interface and the trapping experimental results.

## 2. Results and Discussion

### 2.1. Structure and Composition of $\text{Ag}_3\text{PO}_4/\text{g-C}_3\text{N}_4$ Photocatalysts

Figure 1 shows the XRD patterns of the  $\text{g-C}_3\text{N}_4$ ,  $\text{Ag}_3\text{PO}_4$ , and as-prepared  $\text{Ag}_3\text{PO}_4/\text{g-C}_3\text{N}_4$  samples. There are two characteristic peaks at  $13.1^\circ$  and  $27.5^\circ$  in the XRD pattern of  $\text{g-C}_3\text{N}_4$ , which correspond to the (100) and (002) planes, respectively, (JCPDS files: 87-1526) [35]. All diffraction peaks of the as-prepared  $\text{Ag}_3\text{PO}_4$  coincide with the cubic  $\text{Ag}_3\text{PO}_4$  (JCPDS No. 06-0505) [24]. The  $\text{Ag}_3\text{PO}_4/\text{g-C}_3\text{N}_4$  composites exhibited diffraction peaks corresponding to  $\text{g-C}_3\text{N}_4$  and  $\text{Ag}_3\text{PO}_4$ . By increasing the content of the  $\text{Ag}_3\text{PO}_4$ , its diffraction peaks gradually intensified at the expense of the  $\text{g-C}_3\text{N}_4$  peaks, thus reflecting their contents in the  $\text{Ag}_3\text{PO}_4/\text{g-C}_3\text{N}_4$  hybrids. The XRD analysis also confirmed the high purity of the  $\text{Ag}_3\text{PO}_4$  and  $\text{g-C}_3\text{N}_4$ .

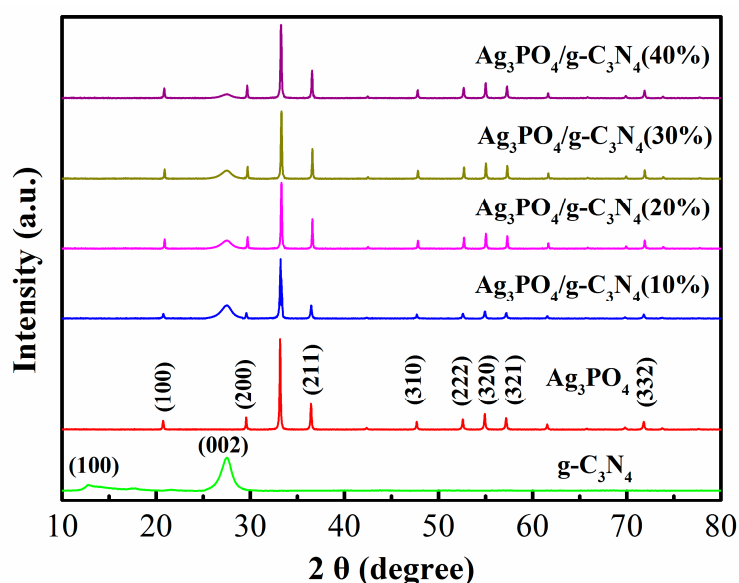


**Figure 1.** X-ray diffraction patterns of  $\text{g-C}_3\text{N}_4$ ,  $\text{Ag}_3\text{PO}_4$ , and  $\text{Ag}_3\text{PO}_4/\text{g-C}_3\text{N}_4$  (X) composites.

The FTIR spectra of the as-prepared sample are shown in Figure 2. For the pure  $\text{g-C}_3\text{N}_4$ , two main absorption regions are clearly observed, the strong absorption bands in the  $1200\text{--}1650\text{ cm}^{-1}$  region were ascribed to the typical skeletal stretching vibration modes of the s-triazine or tri-s-triazine, which corresponded to the CN heterocycles [22]. The sharp peak centered at  $808\text{ cm}^{-1}$  indicated a characteristic breathing mode of the triazine units, and verified that the prepared photocatalyst was a  $\text{g-C}_3\text{N}_4$  or  $\text{g-C}_3\text{N}_4$ -based catalyst [36–38]. For  $\text{Ag}_3\text{PO}_4$ , the observed strong peak at  $546\text{ cm}^{-1}$  was related to the O=P-O bending vibration, while the peak at  $860\text{ cm}^{-1}$  was assigned to the symmetric and asymmetric vibration modes of P-O-P [39]. All of the characteristic peaks of  $\text{g-C}_3\text{N}_4$  and  $\text{Ag}_3\text{PO}_4$  could be observed in the spectra of  $\text{Ag}_3\text{PO}_4/\text{g-C}_3\text{N}_4$  composites, and the intensity of the peaks at  $546\text{ cm}^{-1}$  and  $860\text{ cm}^{-1}$  rose with the increase of  $\text{Ag}_3\text{PO}_4$  content.

The morphology and microstructure of  $\text{Ag}_3\text{PO}_4/\text{g-C}_3\text{N}_4$  were investigated by SEM and TEM. As shown in Figure 3a,b, the C, N, O, P, and Ag elements were all detected in the  $\text{Ag}_3\text{PO}_4/\text{g-C}_3\text{N}_4$  by the element mapping results, which indicated  $\text{Ag}_3\text{PO}_4$  nanoparticles were deposited on the surface of  $\text{g-C}_3\text{N}_4$  and the heterojunction was formed. In order to further confirm the combination of  $\text{Ag}_3\text{PO}_4$  and  $\text{g-C}_3\text{N}_4$ , EDS analysis was further used, as shown in Figure S1. Figure 3c,d are the TEM images of  $\text{g-C}_3\text{N}_4$  and  $\text{Ag}_3\text{PO}_4/\text{g-C}_3\text{N}_4$ , respectively. According to previous research [40], the light part is  $\text{g-C}_3\text{N}_4$ , and the dark part is  $\text{Ag}_3\text{PO}_4$ , which further demonstrates that  $\text{Ag}_3\text{PO}_4$  was well-deposited on the surface of  $\text{g-C}_3\text{N}_4$ . The SEM and TEM images of  $\text{Ag}_3\text{PO}_4$ ,  $\text{Ag}_3\text{PO}_4/\text{g-C}_3\text{N}_4$  (20%),  $\text{Ag}_3\text{PO}_4/\text{g-C}_3\text{N}_4$

(40%) are shown in Figure S2 in the Supplementary Materials. With the increasing ratio of  $\text{Ag}_3\text{PO}_4$  in the composites, the size of  $\text{Ag}_3\text{PO}_4$  nanoparticles increased slightly following an aggregation.

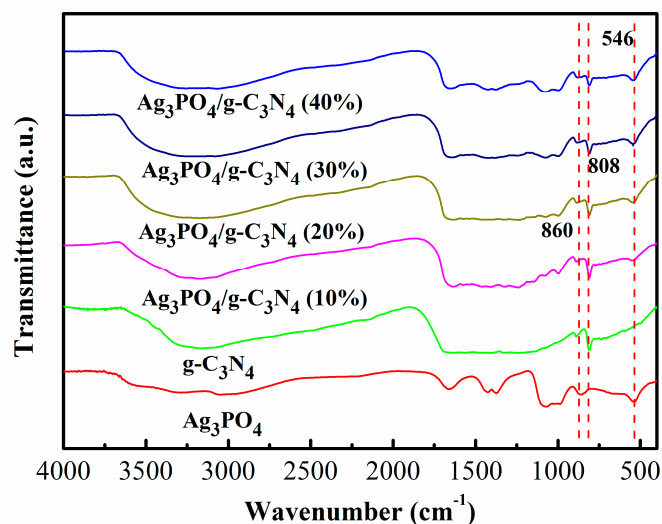


**Figure 2.** FTIR spectra of the as-prepared  $\text{g-C}_3\text{N}_4$ ,  $\text{Ag}_3\text{PO}_4$ , and  $\text{Ag}_3\text{PO}_4/\text{g-C}_3\text{N}_4$  (X) composites.

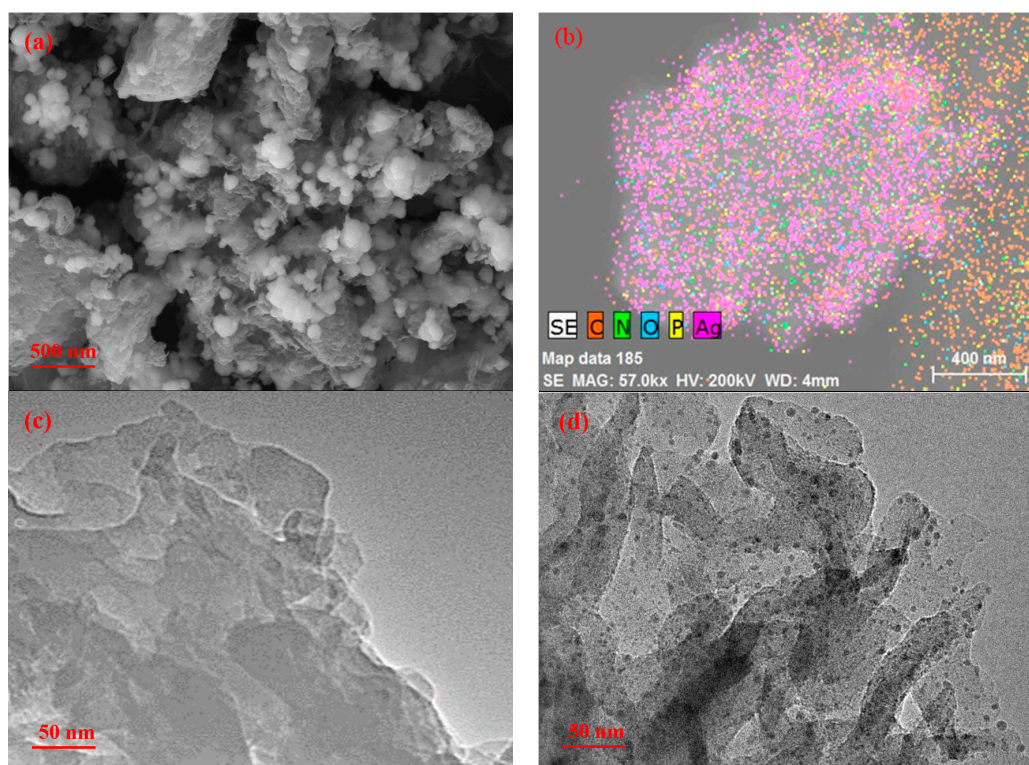


**Figure 3.** (a) SEM image of  $\text{Ag}_3\text{PO}_4/\text{g-C}_3\text{N}_4$  (30%); (b) Element mapping of the  $\text{Ag}_3\text{PO}_4/\text{g-C}_3\text{N}_4$  (30%); (c) TEM image of  $\text{g-C}_3\text{N}_4$ ; and (d) TEM of  $\text{Ag}_3\text{PO}_4/\text{g-C}_3\text{N}_4$  (30%).

Surface chemical states of the  $\text{Ag}_3\text{PO}_4/\text{g-C}_3\text{N}_4$  composite were studied by XPS. Figure 4a shows the XPS spectrum of  $\text{Ag}_3\text{PO}_4/\text{g-C}_3\text{N}_4$  (30%) and  $\text{Ag}_3\text{PO}_4$ . All signals of C, N, Ag, P, and O were detected in the  $\text{Ag}_3\text{PO}_4/\text{g-C}_3\text{N}_4$  composite, which is consistent with the XRD and FTIR results. The typical high-resolution XPS spectra of C 1s, Ag 3d, and P 2d in the composite are shown in Figure 4b–d. C 1s has two peaks at 284.6 and 287.4 eV that are separately attributed to the adventitious

carbon and the  $sp^2$ -hybridized C of N-C=N in  $g-C_3N_4$  [41,42]. The Ag 3d<sub>5/2</sub> and 3d<sub>3/2</sub> of  $Ag_3PO_4$  were located at 367.8 and 373.8 eV, which are consistent with the value of  $Ag^+$  in the  $Ag_3PO_4$  [43]. The P 2p has a peak at 132.4 eV, corresponding to  $P^{5+}$  in the  $Ag_3PO_4$  [15].

The optical properties of the prepared photocatalysts were measured via UV-vis DRS. As shown in Figure 5a, the absorption edge of pure  $g-C_3N_4$  and  $Ag_3PO_4$  is approximately 460 and 505 nm, respectively, indicating that both the  $g-C_3N_4$  and  $Ag_3PO_4$  could absorb solar energy. Based on the Kubelka–Munk function, the plots of  $(Ah\nu)^{1/2}$  vs.  $h\nu$  for  $g-C_3N_4$ ,  $Ag_3PO_4$ , and  $Ag_3PO_4/g-C_3N_4$  (30%) are shown in Figure 5b [5]. The indirect band gap energies of the  $g-C_3N_4$  and  $Ag_3PO_4$  are 2.70 and 2.45 eV, respectively, which is consistent with previous results [13,44]. Compared to  $g-C_3N_4$ , the  $Ag_3PO_4/g-C_3N_4$  (X) composites show an intense and broad background absorption in the visible-light region from 300 to 500 nm, which means that the visible-light absorption ability of the  $Ag_3PO_4/g-C_3N_4$  (X) was improved.

Figure 6 displays the PL spectra of  $Ag_3PO_4/g-C_3N_4$  (X) composites and  $g-C_3N_4$  at an excitation wavelength of 368 nm. Compared with the  $g-C_3N_4$ , the  $Ag_3PO_4/g-C_3N_4$  (X) composites showed significant PL quenching as a result of the efficient charge transfer at the heterostructure interface. In particular, when the molar ratio of  $Ag_3PO_4$  to  $g-C_3N_4$  was 30%, the PL peak in the  $Ag_3PO_4/g-C_3N_4$  (30%) reached the lowest intensity, indicating the most effective inhibition for the recombination of photogenerated electron-hole pairs.

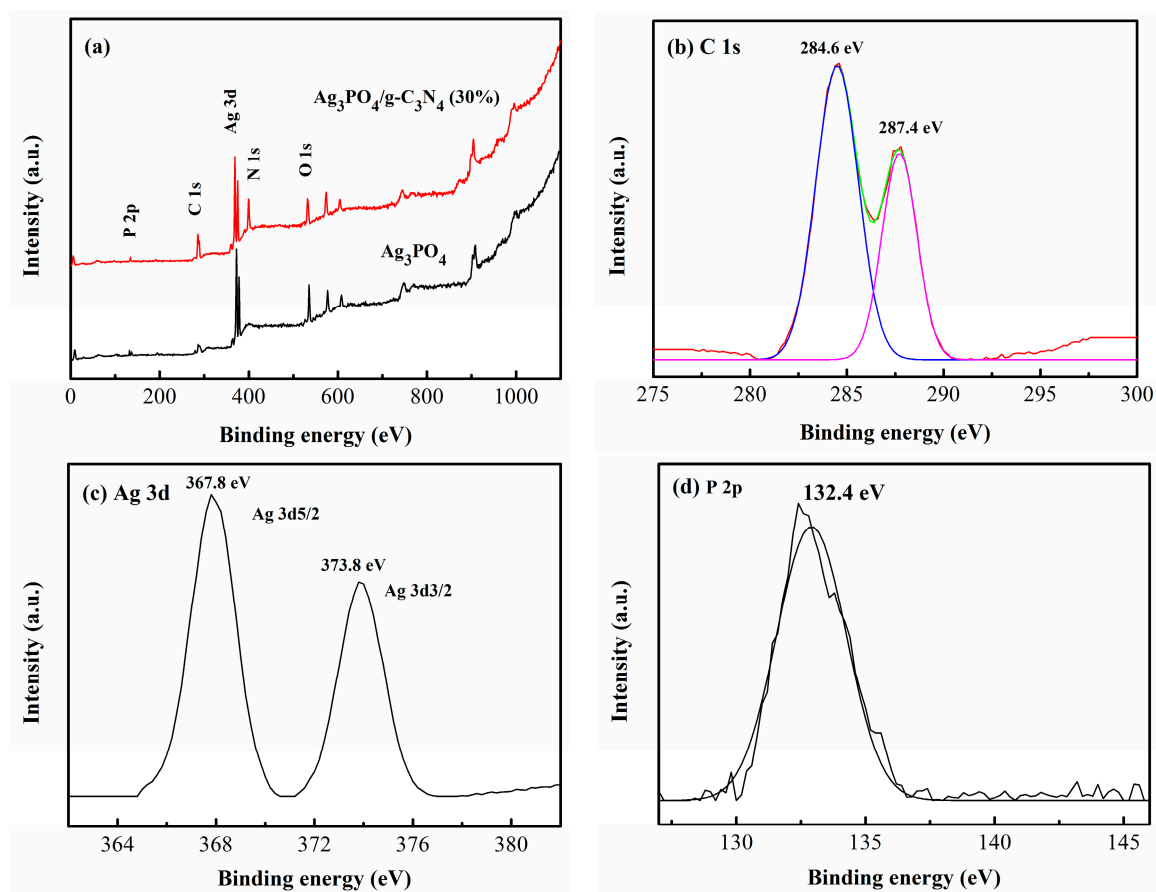


**Figure 4.** XPS spectrum of the  $Ag_3PO_4$  and  $Ag_3PO_4/g-C_3N_4$ : (a) survey spectrum; (b) C 1s; (c) Ag 3d; and (d) P 2p.

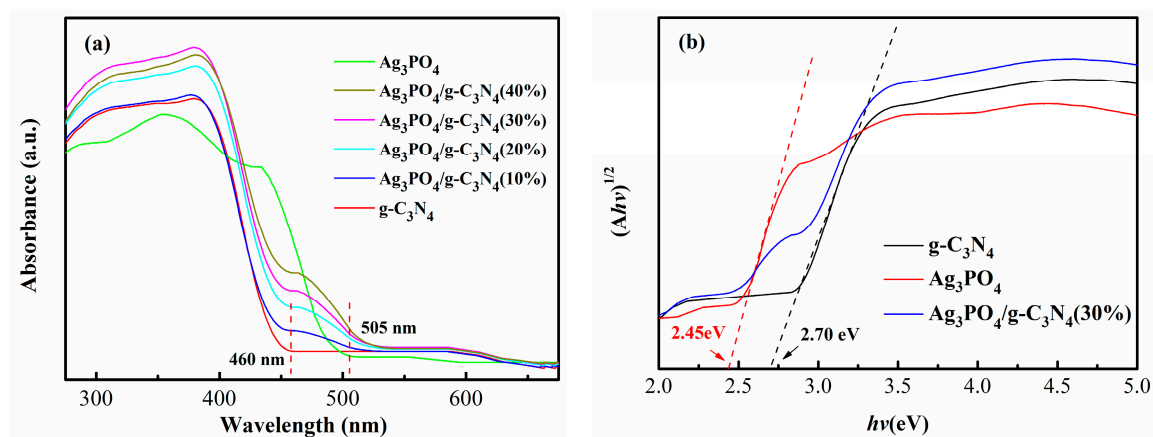


**Figure 5.** (a) UV-Vis diffused reflectance spectra of the as-prepared photocatalyst; (b) Plots of  $(Ah\nu)^{1/2}$  versus energy ( $h\nu$ ) for the  $g\text{-C}_3\text{N}_4$  and  $\text{Ag}_3\text{PO}_4/g\text{-C}_3\text{N}_4$  (30%).

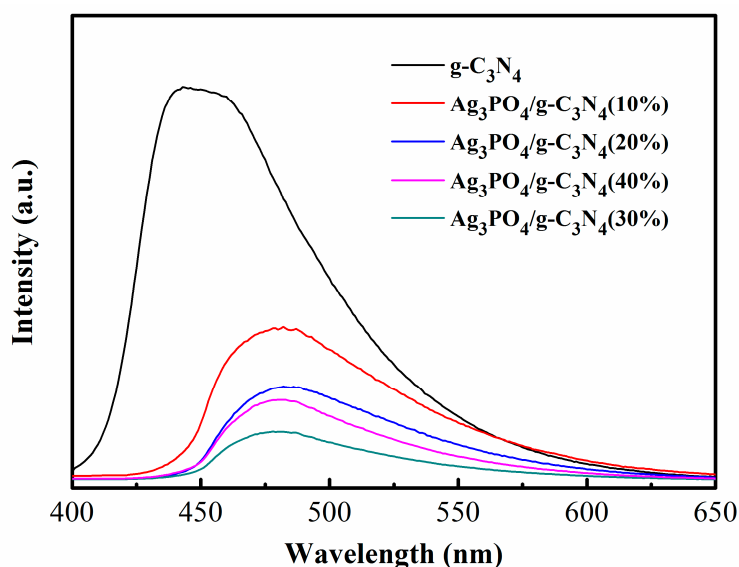


**Figure 6.** PL spectra of  $g\text{-C}_3\text{N}_4$  and  $\text{Ag}_3\text{PO}_4/g\text{-C}_3\text{N}_4$  (X).

## 2.2. Photocatalytic Activity of the $\text{Ag}_3\text{PO}_4/g\text{-C}_3\text{N}_4$ Composites

The photocatalytic activities of the as-prepared  $\text{Ag}_3\text{PO}_4/g\text{-C}_3\text{N}_4$  (X) composites were evaluated by the photodegradation of DCF under visible light. For comparison, the activities of pure  $g\text{-C}_3\text{N}_4$  and  $\text{Ag}_3\text{PO}_4$  were also tested under the same conditions. As shown in Figure 7a, all of the  $\text{Ag}_3\text{PO}_4/g\text{-C}_3\text{N}_4$  (X) composites show a higher photocatalytic degradation rate than the  $g\text{-C}_3\text{N}_4$  and  $\text{Ag}_3\text{PO}_4$ , and the photocatalytic activities are closely related to the molar ratio of  $\text{Ag}_3\text{PO}_4$  to  $g\text{-C}_3\text{N}_4$ . With the increase of  $\text{Ag}_3\text{PO}_4$  doped proportion from 10% to 30% in the composites, the photocatalytic property of the  $\text{Ag}_3\text{PO}_4/g\text{-C}_3\text{N}_4$  composite increased gradually, while further increasing the mass ratio to 40%, which led to a decrease in the photocatalytic activity. The reason may be due to excessive deposits of  $\text{Ag}_3\text{PO}_4$  shielding the active site on  $g\text{-C}_3\text{N}_4$  surfaces, which will subsequently cause a decrease in the photocatalytic activity. To investigate the DCF degradation kinetics, a pseudo-first-order reaction model was used to describe the experimental data. It was found that the photocatalytic DCF degradation followed the first-order kinetics, and the rate constant for the different photocatalysts is shown in Figure 7b. The  $\text{Ag}_3\text{PO}_4/g\text{-C}_3\text{N}_4$  (30%) composite exhibited the highest DCF photodegradation rate ( $0.453 \text{ min}^{-1}$ ), which was 34.8 and 6.4 times faster than those of the  $g\text{-C}_3\text{N}_4$  ( $0.013 \text{ min}^{-1}$ ) and  $\text{Ag}_3\text{PO}_4$

( $0.071 \text{ min}^{-1}$ ), respectively. Several studies have investigated DCF removal in the advanced oxidation processes. Michael observed an 80% DCF (the initial concentration was  $10 \text{ mg L}^{-1}$ ) removal efficiency in 120 min with  $\text{TiO}_2$  as the catalyst under a sonocatalytic process [45]. Shan found that 80% DCF (the initial concentration was  $20 \text{ mg L}^{-1}$ ) was removed in 40 min with  $\text{FeCeO}_x$  under an ultrasonic system [46]. Cheng found that the photodegradation rate of DCF (the initial concentration was  $5 \text{ mg L}^{-1}$ ) was  $0.08945 \text{ h}^{-1}$  with Pd/TNTs photoelectrode under xenon lamp irradiation [47]. Shan has studied the degradation of DCF in a Fenton like system,  $\text{FeCeO}_x\text{-H}_2\text{O}_2$  in detail, and the reaction rate constant of DCF degradation was  $0.073 \text{ min}^{-1}$  [48]. Liu has found that the rate constant of DCF (initial concentration was  $10 \text{ mg L}^{-1}$ ) degradation was  $1.0498 \text{ h}^{-1}$  in a  $\text{Bi}_2\text{MoO}_6/\text{Cu}/\text{PEC}/\text{PS}$  system [49]. Horiya has reported the degradation of DCF (the initial concentration was  $10 \text{ mg L}^{-1}$ ) with mont-La(6%)- $\text{Cu}_{0.6}\text{Cd}_{0.4}\text{S}$  under NUV-Vis irradiation, and the removal of DCF was ca. 92% in 240 min [50]. Martinez has studied the degradation of DCF (the initial concentration was  $8 \text{ mg L}^{-1}$ ) under UV irradiation, and the optimal conditions for a complete removal were obtained using synthesized anatase ( $0.5 \text{ g L}^{-1}$ ) and 50%  $\text{O}_2$  ( $v/v$ ) under UV irradiation, with rate constants ca.  $0.9 \text{ min}^{-1}$  (half-life time ca.  $0.8 \text{ min}^{-1}$ ) [51]. Thus, the obtained results in this study indicated that DCF photodegradation by  $\text{Ag}_3\text{PO}_4/\text{g-C}_3\text{N}_4$  (30%) under visible-light irradiation illustrated an excellent performance for DCF removal.

Since it was quite possible that the intermediate products during the photocatalytic process were more poisonous, the removal of TOC was used to indicate the degree of mineralization of DCF degradation. As shown in Figure 8, DCF was completely decomposed in the first 12 min, while the removal of TOC was only 43.2%, indicated the DCF was completely degraded but partly mineralized.

The stability and reusability of the  $\text{Ag}_3\text{PO}_4/\text{g-C}_3\text{N}_4$  composites were also examined to provide insight into the practical applications. A five-run cycling test of DCF degradation was performed to evaluate the changes of the DCF photodegradation kinetics. Figure 9 shows no apparent decrease in the DCF degradation rate over the five consecutive cycles (totaling 75 min), indicating good photocatalyst stability. Furthermore, the leaching of  $\text{Ag}^+$  after each re-cycle was analyzed by an inductively coupled plasma optical emission spectrometer (ICP-OES), and the result was shown in Table S1.

Furthermore, the XRD patterns of the  $\text{Ag}_3\text{PO}_4/\text{g-C}_3\text{N}_4$  (30%) before and after the photocatalytic reaction were studied to evaluate structural stability. As shown in Figure 10, several small diffraction peaks of Ag that formed from the reduction of  $\text{Ag}_3\text{PO}_4$  appear in the XRD pattern without evident crystalline structure changes during the reaction. From the SEM and TEM images of the cycled  $\text{Ag}_3\text{PO}_4/\text{g-C}_3\text{N}_4$  (30%), shown in Figure S3, there was no significant change in the morphology and microstructure before and after the reaction.

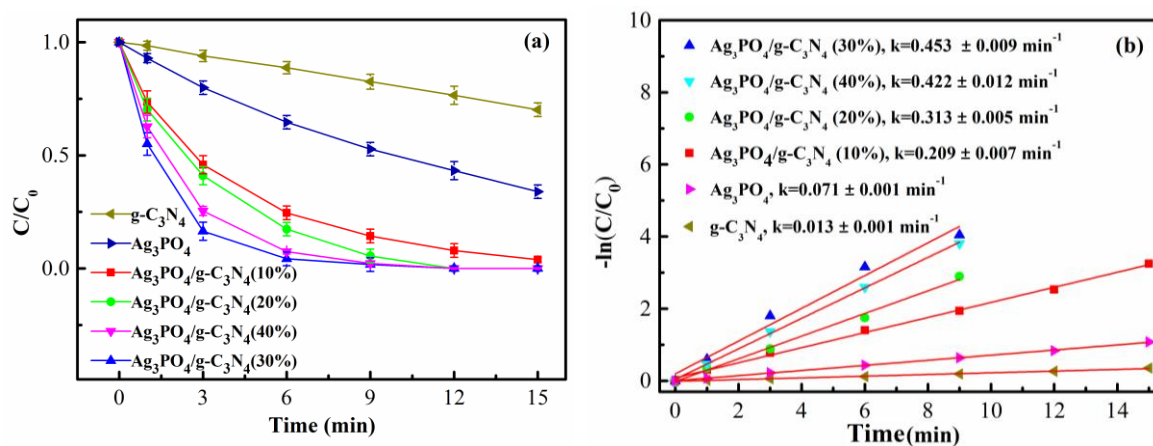


**Figure 7.** (a) DCF photodegradation with different photocatalysts,  $[\text{DCF}] = 1 \text{ mg L}^{-1}$ ,  $[\text{photocatalyst}] = 0.1 \text{ g L}^{-1}$ ; (b) The kinetic constants of  $\text{g-C}_3\text{N}_4$ ,  $\text{Ag}_3\text{PO}_4$ , and  $\text{Ag}_3\text{PO}_4/\text{g-C}_3\text{N}_4$  (X) for the DCF photodegradation.

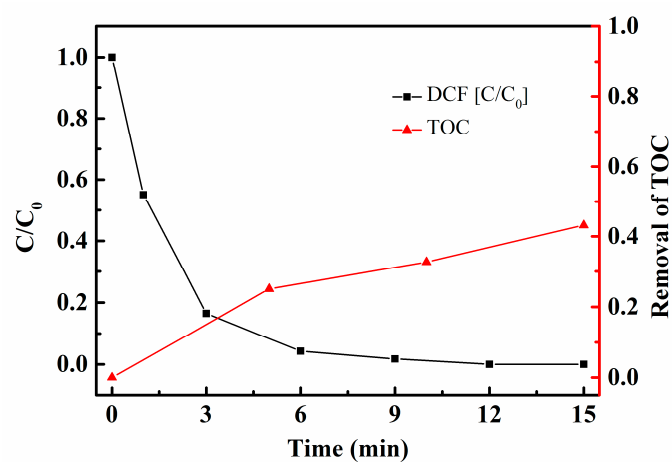


**Figure 8.** The photodegradation of DCF and the TOC removal during the reaction. [DCF] = 1 mg L<sup>-1</sup>, [Ag<sub>3</sub>PO<sub>4</sub>/g-C<sub>3</sub>N<sub>4</sub> (30%)] = 0.1 g L<sup>-1</sup>.

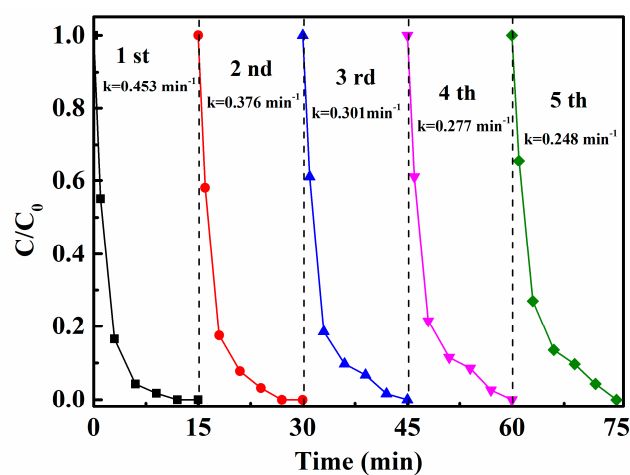


**Figure 9.** Circling runs for the DCF photodegradation in the presence of Ag<sub>3</sub>PO<sub>4</sub>/g-C<sub>3</sub>N<sub>4</sub> (30%) under visible-light irradiation. [DCF] = 1 mg L<sup>-1</sup>, [Ag<sub>3</sub>PO<sub>4</sub>/g-C<sub>3</sub>N<sub>4</sub> (30%)] = 0.1 g L<sup>-1</sup>.

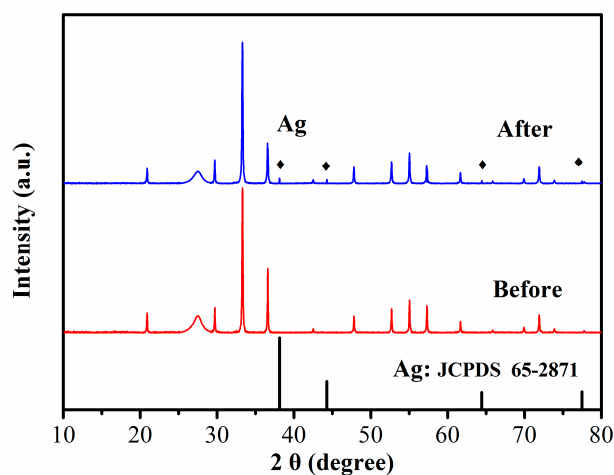
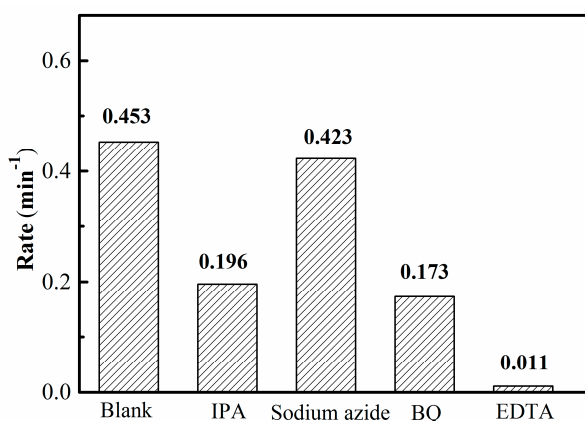


**Figure 10.** XRD patterns of Ag<sub>3</sub>PO<sub>4</sub>/g-C<sub>3</sub>N<sub>4</sub> (30%) before and after the photocatalytic reaction.

### 2.3. Possible Photocatalytic Mechanisms

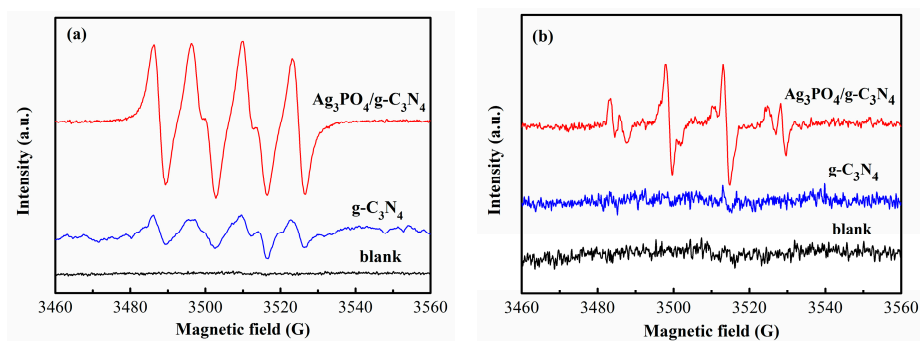
#### 2.3.1. The Roles of ROS

Figure 11 shows the effects of different scavengers for the DCF photodegradation with  $\text{Ag}_3\text{PO}_4/\text{g-C}_3\text{N}_4$  (30%) under visible light irradiation. Adding sodium azide did not appreciably inhibit the degradation rate of DCF, while the addition of isopropanol, benzoquinone, and disodium EDTA decreased the DCF degradation rate from 0.453 to 0.196, 0.173, and 0.011  $\text{min}^{-1}$ , respectively, indicating that  $\cdot\text{OH}$ ,  $\cdot\text{O}_2^-$  and  $\text{h}^+$  were all responsible for ROS during the photocatalytic processes.



**Figure 11.** The effects of different scavengers for the DCF photodegradation with  $\text{Ag}_3\text{PO}_4/\text{g-C}_3\text{N}_4$  (30%) under visible-light irradiation.

In order to further verify the active species in the photocatalytic reaction, the existence of  $\cdot\text{O}_2^-$  and  $\cdot\text{OH}$  was detected by ESR [24]. In Figure 12a,b, it can be seen that no characteristic peaks of  $\text{DMPO}\cdot\text{O}_2^-$  and  $\text{DMPO}\cdot\text{OH}$  adducts were generated without light irradiation, while the characteristic peaks of the  $\text{DMPO}\cdot\text{O}_2^-$  and  $\text{DMPO}\cdot\text{OH}$  adducts were observed over the  $\text{Ag}_3\text{PO}_4/\text{g-C}_3\text{N}_4$  under visible light irradiation, which proves that the  $\cdot\text{O}_2^-$  and  $\cdot\text{OH}$  radicals were indeed generated and played an important role during the reaction. Moreover, compared with  $\text{Ag}_3\text{PO}_4/\text{g-C}_3\text{N}_4$ , the intensities of the  $\text{DMPO}\cdot\text{O}_2^-$  peaks were lower and no  $\text{DMPO}\cdot\text{OH}$  peaks could be found, indicating that less  $\text{O}_2^-$  and no  $\cdot\text{OH}$  were generated in the reaction process over  $\text{g-C}_3\text{N}_4$ .



**Figure 12.** ESR signals of (a)  $\text{DMPO}\cdot\text{O}_2^-$  in methanol dispersion; and (b)  $\text{DMPO}\cdot\text{OH}$  in aqueous dispersion with visible-light irradiation.

#### 2.3.2. Proposed Mechanisms

From the result of the trapping experiment,  $\text{OH}$ ,  $\cdot\text{O}_2^-$  and  $\text{h}^+$  were all responsible for ROS during the photocatalytic processes, from the result of ESR,  $\cdot\text{O}_2^-$  and  $\cdot\text{OH}$  radicals were indeed generated

and played an important role during the reaction. Generally speaking, there are two types of electron separation processes for the photogenerated electron-hole pairs during the photocatalytic reaction, one is a double-transfer mechanism and the other is a Z-scheme mechanism. The double-transfer mechanism is a common separation process for a large amount of composite photocatalysts, such as  $\text{Ag}_2\text{O}/\text{g-C}_3\text{N}_4$  composites [22]. If the  $\text{Ag}_3\text{PO}_4/\text{g-C}_3\text{N}_4$  heterojunctions follow this mechanism, the schematic diagram of  $\text{Ag}_3\text{PO}_4/\text{g-C}_3\text{N}_4$  can be seen in Figure 13a, as the potentials of the CB and VB edges of the  $\text{g-C}_3\text{N}_4$  are  $-1.30$  eV and  $+1.40$  eV (vs. NHE), respectively, and the CB and VB edge potentials of the  $\text{Ag}_3\text{PO}_4$  are  $+0.45$  eV and  $+2.90$  eV (vs. NHE), respectively [52,53]. Electrons in the CB of  $\text{g-C}_3\text{N}_4$  would transfer to that of the  $\text{Ag}_3\text{PO}_4$ , and the holes accumulate on the VB of  $\text{g-C}_3\text{N}_4$ . However, as the CB of the  $\text{Ag}_3\text{PO}_4$  ( $+0.45$  eV, vs. NHE) is more positive than the potentials of the  $\text{O}_2/\cdot\text{O}_2^-$  ( $-0.33$  eV, vs. NHE) [54], the photogenerated electrons on the CB of the  $\text{Ag}_3\text{PO}_4$  cannot reduce the  $\text{O}_2$  to yield  $\cdot\text{O}_2^-$ . In addition, due to the potentials of the  $\cdot\text{OH}/\text{OH}^-$  ( $+2.38$  eV, vs. NHE) and  $\cdot\text{OH}/\text{H}_2\text{O}$  ( $+2.72$  eV, vs. NHE) [55], which are more positive than the VB of  $\text{g-C}_3\text{N}_4$  ( $+1.4$  eV, vs. NHE), the holes on the VB of  $\text{g-C}_3\text{N}_4$  cannot react with the  $\text{OH}^-$  and  $\text{H}_2\text{O}$  to form an  $\cdot\text{OH}$  radical. As this result contradicts the results in the reactive species-trapping experiments, the double-transfer mechanism played a minor or negligible role. In contrast, the electron transfer might follow a direct Z-scheme on the  $\text{Ag}_3\text{PO}_4/\text{g-C}_3\text{N}_4$ . During the photocatalytic reactions,  $\text{Ag}^0$  could be formed through the reduction of  $\text{Ag}_3\text{PO}_4$  by the photoexcited electron that is deposited on the  $\text{Ag}_3\text{PO}_4$  surface. In this scheme, the  $\text{Ag}^0$  nanoparticles could act as a charge transmission bridge to form the  $\text{Ag}_3\text{PO}_4/\text{Ag}/\text{g-C}_3\text{N}_4$  Z-scheme system, which is shown in Figure 13b. The Ag had a relatively low Fermi level ( $E_F = 0.4$  V vs. NHE), which could serve as the electron acceptor for the photoexcited electrons. The photogenerated electrons in the  $\text{Ag}_3\text{PO}_4$  could be rapidly transferred to the  $\text{g-C}_3\text{N}_4$  through  $\text{Ag}^0$  nanoparticles that promote the effective separation of photogenerated electron-hole pairs and suppress the  $\text{Ag}_3\text{PO}_4$  reduction. Simultaneously, the holes in the VB of the  $\text{g-C}_3\text{N}_4$  could move to the  $\text{Ag}^0$  nanoparticles and combine with the electrons. The type of charge transmission could efficiently enhance the electron-hole pairs separation and enable the electrons and holes to remain on the CB of the  $\text{g-C}_3\text{N}_4$  and VB of  $\text{Ag}_3\text{PO}_4$ , respectively. On the other hand, the surface plasmon resonance (SPR) endowed in the Ag nanoparticles could effectively promote the visible-light absorption ability of the  $\text{Ag}_3\text{PO}_4/\text{g-C}_3\text{N}_4$  composite. Furthermore, under this scheme, as the CB of  $\text{g-C}_3\text{N}_4$  ( $-1.30$  eV, vs. NHE) was more negative than the potentials of  $\text{O}_2/\cdot\text{O}_2^-$  ( $-0.33$  eV, vs. NHE), and the VB of  $\text{Ag}_3\text{PO}_4$  ( $2.90$  eV, vs. NHE) was more positive than the potentials of the  $\cdot\text{OH}/\text{OH}^-$  ( $2.38$  eV, vs. NHE) and the  $\cdot\text{OH}/\text{H}_2\text{O}$  ( $2.72$  eV, vs. NHE), the photogenerated electrons on the CB of  $\text{g-C}_3\text{N}_4$  could reduce the  $\text{O}_2$  to yield  $\cdot\text{O}_2^-$ . The enriched holes on the VB of  $\text{Ag}_3\text{PO}_4$  could react with the  $\text{OH}^-$  or  $\text{H}_2\text{O}$  to form  $\cdot\text{OH}$  radicals, which is consistent with the trapping experimental results.

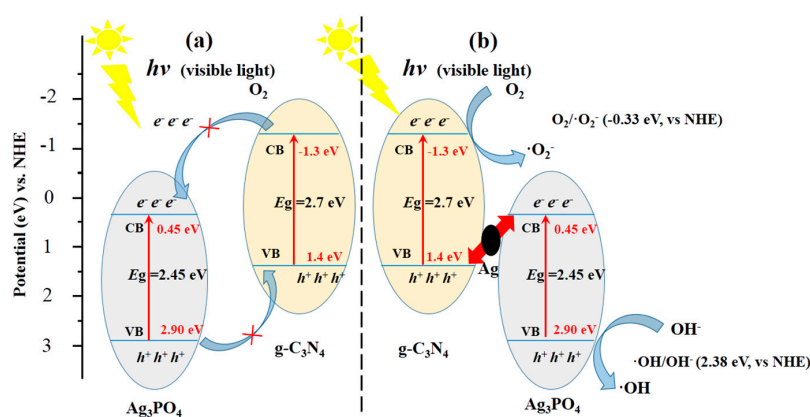


**Figure 13.** Schematic diagram of the photoexcited electron-hole transfer process (a) Double-transfer mechanism; and (b) Z-scheme mechanism.

### 3. Experimental

#### 3.1. Materials

All chemicals were used as received without any further purification. Melamine ( $C_3H_6N_6$ ), silver nitrate ( $AgNO_3$ ), and sodium dihydrogen phosphate ( $NaH_2PO_4$ ) were purchased from Sinopharm Chemical Reagent Corp. (Beijing, China). Diclofenac sodium was purchased from Sigma Chemical Reagent Co. (St. Louis, MO, USA).

#### 3.2. Preparation of the Photocatalysts

##### 3.2.1. Synthesis of g- $C_3N_4$

Graphitic carbon nitride (g- $C_3N_4$ ) was synthesized according to previous reports in the literature [56]. Typically, 10 g of acid-treated melamine was put in a muffle furnace and heated at a ramping rate of  $4\text{ }^\circ\text{C min}^{-1}$  from room temperature to  $550\text{ }^\circ\text{C}$ , and then kept at  $550\text{ }^\circ\text{C}$  for 4 h.

##### 3.2.2. Synthesis of $Ag_3PO_4/g-C_3N_4$ Composite

g- $C_3N_4$  nanosheets (0.1 g) were added to 100 mL of deionized water and ultrasonicated for 20 min. Different amounts of  $[Ag(NH_3)_2]^+$  solution were then added to the g- $C_3N_4$  mixture and magnetically stirred for 30 min. Finally,  $NaH_2PO_4$  was added to the mixture solution under vigorous stirring. After 3 h, the product was collected by filtration, washed with deionized water, and dried in an oven at  $70\text{ }^\circ\text{C}$  for 10 h. The obtained samples were denoted as  $Ag_3PO_4/g-C_3N_4$  (X), where X (10%, 20%, 30%, or 40%) represents the molar ratio of  $Ag_3PO_4$  to g- $C_3N_4$  in  $Ag_3PO_4/g-C_3N_4$ . The  $Ag_3PO_4$  sample was prepared following the same procedures, excluding the addition of g- $C_3N_4$ .

#### 3.3. Characterization of the As-Prepared Photocatalysts

The phase purity and crystal structure of the obtained samples were examined by X-ray diffraction (XRD) using a Bruker D8 Advance X-ray Diffractometer (Billerica, MA, USA) equipped with Cu-K $\alpha$  radiation ( $\lambda = 1.5406\text{ \AA}$ ) in the  $2\theta$  range of  $10^\circ$  to  $80^\circ$ . The photocatalyst chemical structures were confirmed by a Nicolet 5700 Fourier transform-infrared spectrometer (Thermo Fisher Scientific, WI, USA) with a scanning range from  $4000$  to  $400\text{ cm}^{-1}$  at room temperature. An observation by transmission electron microscope (TEM) was taken with a JEOL-JEM-2100 (JEOL, Akishima, Tokyo, Japan) operated at up to 200 kV. Observations from a scanning electron microscope (SEM) and an energy dispersive spectrometer (EDS) were taken using a Hitachi S4800 (Hitachi, Tokyo, Japan). Surface composition and chemical bonds were examined with a PHI 5000C ESCA X-ray photoelectron spectroscopy (XPS). UV-Vis diffuse reflectance spectra (UV-Vis DRS) were obtained on an UV-Vis spectrophotometer (UV-2550, Shimadzu, Kyoto, Japan).  $BaSO_4$  was used as a reflectance standard in the UV-Vis diffuse reflectance experiments. Photoluminescence spectroscopy (PL) of the samples was obtained on a Horiba FL-3000 spectrofluorometer with a 368 nm excitation wavelength. The scanning speed was  $1200\text{ nm min}^{-1}$ , and the photomultipliers' voltage was 700 V. Electron spin resonance (ESR) of the spin-trapped paramagnetic species with DMPO were tested by the Bruker Elexsys E500 spectrometer (Billerica, MA, USA).

#### 3.4. Experimental Procedures

The photocatalyst performance was evaluated through DCF photocatalytic degradation under visible light. The source of radiation was a 300 W Xenon lamp (BL-GHX-Xe-300, Shanghai, China) with a suitable optical cut-off filter ( $\lambda \geq 400\text{ nm}$ ), and the temperature of the solution was maintained at  $25\text{ }^\circ\text{C}$  with a jacketed cooler. In a typical experiment, 10 mg of the photocatalyst was suspended in 100 mL of DCF aqueous solution ( $1\text{ mg L}^{-1}$ ) in a quartz reactor. The photocatalytic tests were performed with magnetic stirring. During the reaction, the aqueous samples were collected at given time intervals and filtrated through  $0.22\text{ }\mu\text{m}$  polyether sulfone membranes. The DCF concentration was measured

by a high-performance liquid chromatography (HPLC) system (Agilent 1200, Santa Clara, CA, USA). The analytical column was a C18 column (Gemini 5  $\mu\text{m}$ , 150 mm  $\times$  4.6 mm, from Phenomenex, Torrance, CA, USA). The mobile phase consisted of a mixture of 80% methanol and 20% water at a constant flow rate of 1.0 mL  $\text{min}^{-1}$ , and the detection wavelength was set at 276 nm.

To test the stability and reusability of the photocatalyst, cyclic experiments of DCF photodegradation were conducted. After each cycle, the photocatalyst was filtered through 0.22  $\mu\text{m}$  polyether sulfone membranes and washed several times with deionized water for the subsequent cycle.

#### 4. Conclusions

In summary, a series of novel visible-light-driven  $\text{Ag}_3\text{PO}_4/\text{g-C}_3\text{N}_4$  (X) composites were prepared by a deposition-precipitation method. The as-prepared photocatalyst exhibited excellent photocatalysis for DCF degradation, which was much higher than that of pure  $\text{g-C}_3\text{N}_4$  and  $\text{Ag}_3\text{PO}_4$ . The DCF photodegradation under visible light irradiation followed first-order kinetics; when the molar ratio of  $\text{Ag}_3\text{PO}_4$  and  $\text{g-C}_3\text{N}_4$  was 30%, the composites showed optimal photocatalytic performance, and the reaction rate constant on  $\text{Ag}_3\text{PO}_4/\text{g-C}_3\text{N}_4$  (30%) was 0.453  $\text{min}^{-1}$ , which was almost 17.9 and 6.4-time as much as that of pure  $\text{g-C}_3\text{N}_4$  and  $\text{Ag}_3\text{PO}_4$ , respectively. The enhanced photocatalytic activity of the  $\text{Ag}_3\text{PO}_4/\text{g-C}_3\text{N}_4$  could be beneficial for the heterojunction formed between  $\text{g-C}_3\text{N}_4$  and  $\text{Ag}_3\text{PO}_4$ , as well as to the SPR effects of formed  $\text{Ag}^0$  nanoparticles during the reaction. Based on the energy band position and the trapping experimental results, it was found that the electron transfer style of the  $\text{Ag}_3\text{PO}_4/\text{g-C}_3\text{N}_4$  followed the Z-scheme mechanism. This study provides a new idea in the design of heterojunction photocatalysts for the photodegradation of NSAIDs in aquatic environments.

**Supplementary Materials:** The following are available online at <http://www.mdpi.com/xxx/s1>, Figure S1: EDS analysis of  $\text{Ag}_3\text{PO}_4/\text{g-C}_3\text{N}_4$  (30%), Figure S2: SEM images of (a)  $\text{Ag}_3\text{PO}_4$ , (c)  $\text{Ag}_3\text{PO}_4/\text{g-C}_3\text{N}_4$  (20%) and (e)  $\text{Ag}_3\text{PO}_4/\text{g-C}_3\text{N}_4$  (40%), and TEM images (b)  $\text{Ag}_3\text{PO}_4$ , (d)  $\text{Ag}_3\text{PO}_4/\text{g-C}_3\text{N}_4$  (20%) and (f)  $\text{Ag}_3\text{PO}_4/\text{g-C}_3\text{N}_4$  (40%), Figure S3: SEM and TEM images of  $\text{Ag}_3\text{PO}_4/\text{g-C}_3\text{N}_4$  (30%) after the reaction, Table S1: The concentration of  $\text{Ag}^+$  after each re-cycle test.

**Acknowledgments:** This study was supported by State Key Laboratory of Pollution Control and Resource Reuse Foundation (PCRRY16001), and Major Science and Technology Program for Water Pollution Control and Treatment (2017ZX07501001), China. We are grateful to the Key Laboratory of Yangtze River Water Environment, Ministry of Education, for providing facilities for the experiments and the analysis.

**Author Contributions:** For research articles with several authors, a short paragraph specifying their individual contributions must be provided. The following statements should be used “Wei Zhang, Jun Shi and Huiping Deng conceived and designed the experiments; Wei Zhang performed the experiments; Wei Zhang and Jun Shi analyzed the data; Li Zhou contributed reagents/materials/analysis tools; Wei Zhang wrote the paper.” Authorship must be limited to those who have contributed substantially to the work reported.

**Conflicts of Interest:** The authors declare no conflict of interest.

#### References

1. Ma, S.; Zhan, S.; Jia, Y.; Zhou, Q. Highly efficient antibacterial and Pb(II) removal effects of Ag-CoFe<sub>2</sub>O<sub>4</sub>-Go nanocomposite. *ACS Appl. Mater. Interfaces* **2015**, *7*, 10576–10586. [[CrossRef](#)] [[PubMed](#)]
2. Taqieddin, E.; Amiji, M. Enzyme immobilization in novel alginate–chitosan core-shell microcapsules. *Biomaterials* **2004**, *25*, 1937–1945. [[CrossRef](#)] [[PubMed](#)]
3. Wang, F.; Zhang, K. Reduced graphene oxide–TiO<sub>2</sub> nanocomposite with high photocatalytic activity for the degradation of Rhodamine B. *J. Mol. Catal. A Chem.* **2011**, *345*, 101–107. [[CrossRef](#)]
4. Kondo, K.; Murakami, N.; Ye, C.; Tsubota, T.; Ohno, T. Development of highly efficient sulfur-doped TiO<sub>2</sub> photocatalysts hybridized with graphitic carbon nitride. *Appl. Catal. B Environ.* **2013**, *142–143*, 362–367. [[CrossRef](#)]
5. Dong, F.; Zhao, Z.; Xiong, T.; Ni, Z.; Zhang, W.; Sun, Y.; Ho, W.K. In situ construction of  $\text{g-C}_3\text{N}_4/\text{g-C}_3\text{N}_4$  metal-free heterojunction for enhanced visible-light photocatalysis. *ACS Appl. Mater. Interfaces* **2013**, *5*, 11392–11401. [[CrossRef](#)] [[PubMed](#)]

6. Zhang, P.; Wang, Y.; Yao, J.; Wang, C.; Yan, C.; Antonietti, M.; Li, H. Visible-light-induced metal-free allylic oxidation utilizing a coupled photocatalytic system of g-C<sub>3</sub>N<sub>4</sub> and n-hydroxy compounds. *Adv. Synth. Catal.* **2011**, *353*, 1447–1451. [[CrossRef](#)]
7. Zhu, M.; Chen, P.; Liu, M. Graphene oxide wrapped Ag/Ag<sub>x</sub> (X = Br, Cl) nanocomposite as a highly efficient visible-light plasmonic photocatalyst. *ACS Nano* **2011**, *5*, 4529–4536. [[CrossRef](#)] [[PubMed](#)]
8. Wang, Y.; Bai, X.; Pan, C.; He, J.; Zhu, Y. Enhancement of photocatalytic activity of Bi<sub>2</sub>WO<sub>6</sub> hybridized with graphite-like C<sub>3</sub>N<sub>4</sub>. *J. Mater. Chem.* **2012**, *22*, 11568–11573. [[CrossRef](#)]
9. Zhou, P.; Yu, J.; Jaroniec, M. All-solid-state z-scheme photocatalytic systems. *Adv. Mater.* **2014**, *26*, 4920–4935. [[CrossRef](#)] [[PubMed](#)]
10. Tada, H.; Mitsui, T.; Kiyonaga, T.; Akita, T.; Tanaka, K. All-solid-state z-scheme in CdS-Au-TiO<sub>2</sub> three-component nanojunction system. *Nat. Mater.* **2006**, *5*, 782–786. [[CrossRef](#)] [[PubMed](#)]
11. Yi, Z.; Ye, J.; Kikugawa, N.; Kako, T.; Ouyang, S.; Stuartwilliams, H.; Yang, H.; Cao, J.; Luo, W.; Li, Z. An orthophosphate semiconductor with photooxidation properties under visible-light irradiation. *Nat. Mater.* **2010**, *9*, 559–564. [[CrossRef](#)] [[PubMed](#)]
12. Bi, Y.; Ouyang, S.; Umezawa, N.; Cao, J.; Ye, J. Facet effect of single-crystalline Ag<sub>3</sub>PO<sub>4</sub> sub-microcrystals on photocatalytic properties. *J. Am. Chem. Soc.* **2011**, *133*, 6490–6492. [[CrossRef](#)] [[PubMed](#)]
13. Guo, J.; Ouyang, S.; Li, P.; Zhang, Y.; Kako, T.; Ye, J. A new heterojunction Ag<sub>3</sub>PO<sub>4</sub>/Cr-SrTiO<sub>3</sub> photocatalyst towards efficient elimination of gaseous organic pollutants under visible light irradiation. *Appl. Catal. B Environ.* **2013**, *134–135*, 286–292. [[CrossRef](#)]
14. Zhang, F.J.; Xie, F.Z.; Zhu, S.F.; Liu, J.; Zhang, J.; Mei, S.F.; Zhao, W. A novel photofunctional g-C<sub>3</sub>N<sub>4</sub>/Ag<sub>3</sub>PO<sub>4</sub> bulk heterojunction for decolorization of Rh.B. *Chem. Eng. J.* **2013**, *228*, 435–441. [[CrossRef](#)]
15. Chen, F.; Yang, Q.; Li, X.; Zeng, G.; Wang, D.; Niu, C.; Zhao, J.; An, H.; Xie, T.; Deng, Y. Hierarchical assembly of graphene-bridged Ag<sub>3</sub>PO<sub>4</sub>/Ag/BiVO<sub>4</sub>(040) z-scheme photocatalyst: An efficient, sustainable and heterogeneous catalyst with enhanced visible-light photoactivity towards tetracycline degradation under visible light irradiation. *Appl. Catal. B Environ.* **2017**, *200*, 330–342. [[CrossRef](#)]
16. Lu, J.; Wang, Y.; Liu, F.; Zhang, L.; Chai, S. Fabrication of a direct z-scheme type WO<sub>3</sub>/Ag<sub>3</sub>PO<sub>4</sub> composite photocatalyst with enhanced visible-light photocatalytic performances. *Appl. Surf. Sci.* **2017**, *393*, 180–190. [[CrossRef](#)]
17. Yao, W.; Zhang, B.; Huang, C.; Ma, C.; Song, X.; Xu, Q. Synthesis and characterization of high efficiency and stable Ag<sub>3</sub>PO<sub>4</sub>/TiO<sub>2</sub> visible light photocatalyst for the degradation of Methylene Blue and Rhodamine B solutions. *J. Mater. Chem.* **2012**, *22*, 4050–4055. [[CrossRef](#)]
18. Cao, S.; Yu, J. g-C<sub>3</sub>N<sub>4</sub>-based photocatalysts for hydrogen generation. *J. Phys. Chem. Lett.* **2014**, *5*, 2101–2107. [[CrossRef](#)] [[PubMed](#)]
19. Tahir, M.; Cao, C.; Mahmood, N.; Butt, F.K.; Mahmood, A.; Idrees, F.; Hussain, S.; Tanveer, M.; Ali, Z.; Aslam, I. Multifunctional g-C<sub>3</sub>N<sub>4</sub> nanofibers: A template-free fabrication and enhanced optical, electrochemical, and photocatalyst properties. *ACS Appl. Mater. Interfaces* **2014**, *6*, 1258–1265. [[CrossRef](#)] [[PubMed](#)]
20. Niu, P.; Zhang, L.L.; Liu, G.; Cheng, H.M. Graphene-like carbon nitride nanosheets for improved photocatalytic activities. *Adv. Funct. Mater.* **2012**, *22*, 4763–4770. [[CrossRef](#)]
21. Gu, H.; Zhou, T.; Shi, G. Synthesis of graphene supported graphene-like C<sub>3</sub>N<sub>4</sub> metal-free layered nanosheets for enhanced electrochemical performance and their biosensing for biomolecules. *Talanta* **2015**, *132*, 871–876. [[CrossRef](#)] [[PubMed](#)]
22. Xu, M.; Han, L.; Dong, S. Facile fabrication of highly efficient g-C<sub>3</sub>N<sub>4</sub>/Ag<sub>2</sub>O heterostructured photocatalysts with enhanced visible-light photocatalytic activity. *ACS Appl. Mater. Interfaces* **2013**, *5*, 12533–12540. [[CrossRef](#)] [[PubMed](#)]
23. Kumar, S.; Surendar, T.; Baruah, A.; Shanker, V. Synthesis of a novel and stable g-C<sub>3</sub>N<sub>4</sub>/Ag<sub>3</sub>PO<sub>4</sub> hybrid nanocomposite photocatalyst and study of the photocatalytic activity under visible light irradiation. *J. Mater. Chem. A* **2013**, *1*, 5333–5340. [[CrossRef](#)]
24. Meng, S.; Ning, X.; Zhang, T.; Chen, S.F.; Fu, X. What is the transfer mechanism of photogenerated carriers for the nanocomposite photocatalyst Ag<sub>3</sub>PO<sub>4</sub>/g-C<sub>3</sub>N<sub>4</sub>, band-band transfer or a direct z-scheme? *Phys. Chem. Chem. Phys.* **2015**, *17*, 11577–11585. [[CrossRef](#)] [[PubMed](#)]
25. He, P.; Song, L.; Zhang, S.; Wu, X.; Wei, Q. Synthesis of g-C<sub>3</sub>N<sub>4</sub>/Ag<sub>3</sub>PO<sub>4</sub> heterojunction with enhanced photocatalytic performance. *Mater. Res. Bull.* **2014**, *51*, 432–437. [[CrossRef](#)]

26. Xiu, Z.; Bo, H.; Wu, Y.; Hao, X. Graphite-like  $C_3N_4$  modified  $Ag_3PO_4$  nanoparticles with highly enhanced photocatalytic activities under visible light irradiation. *Appl. Surf. Sci.* **2014**, *289*, 394–399. [[CrossRef](#)]
27. He, Y.; Zhang, L.; Teng, B.; Fan, M. New application of z-scheme  $Ag_3PO_4/g-C_3N_4$  composite in converting  $CO_2$  to fuel. *Environ. Sci. Technol.* **2015**, *49*, 649–656. [[CrossRef](#)] [[PubMed](#)]
28. Zhang, Y.; Geissen, S.U.; Gal, C. Carbamazepine and diclofenac: Removal in wastewater treatment plants and occurrence in water bodies. *Chemosphere* **2008**, *73*, 1151–1161. [[CrossRef](#)] [[PubMed](#)]
29. Schwaiger, J.; Ferling, H.; Mallow, U.; Wintermayr, H.; Negele, R.D. Toxic effects of the non-steroidal anti-inflammatory drug diclofenac. Part I: Histopathological alterations and bioaccumulation in rainbow trout. *Aquat. Toxicol.* **2004**, *68*, 141–150. [[CrossRef](#)] [[PubMed](#)]
30. Triebkorn, R.; Casper, H.; Heyd, A.; Eikemper, R.; Köhler, H.R.; Schwaiger, J. Toxic effects of the non-steroidal anti-inflammatory drug diclofenac. Part II: Cytological effects in liver, kidney, gills and intestine of rainbow trout (*oncorhynchus mykiss*). *Aquat. Toxicol.* **2004**, *68*, 151–166. [[CrossRef](#)] [[PubMed](#)]
31. Mehinto, A.C.; Hill, E.M.; Tyler, C.R. Uptake and biological effects of environmentally relevant concentrations of the nonsteroidal anti-inflammatory pharmaceutical diclofenac in rainbow trout (*oncorhynchus mykiss*). *Environ. Sci. Technol.* **2010**, *44*, 2176–2182. [[CrossRef](#)] [[PubMed](#)]
32. Sein, M.M.; Zedda, M.; Tuerk, J.; Schmidt, T.C.; Golloch, A.; Sonntag, C.V. Oxidation of diclofenac with ozone in aqueous solution. *Environ. Sci. Technol.* **2008**, *42*, 6656–6662. [[CrossRef](#)] [[PubMed](#)]
33. Hartmann, J.; Bartels, P.; Mau, U.; Witter, M.; von Tumpling, W.; Hofmann, J.; Nietzschmann, E. Degradation of the drug diclofenac in water by sonolysis in presence of catalysts. *Chemosphere* **2008**, *70*, 453–461. [[CrossRef](#)] [[PubMed](#)]
34. Stulten, D.; Zuhlke, S.; Lamshoft, M.; Spitteller, M. Occurrence of diclofenac and selected metabolites in sewage effluents. *Sci. Total Environ.* **2008**, *405*, 310–316. [[CrossRef](#)] [[PubMed](#)]
35. Cao, J.; Zhao, Y.; Lin, H.; Xu, B.; Chen, S. Ag/AgBr/g- $C_3N_4$ : A highly efficient and stable composite photocatalyst for degradation of organic contaminants under visible light. *Mater. Res. Bull.* **2013**, *48*, 3873–3880. [[CrossRef](#)]
36. Chen, W.; Li, X.; Pan, Z.; Ma, S.; Li, L. Effective mineralization of diclofenac by catalytic ozonation using Fe-MCM-41 catalyst. *Chem. Eng. J.* **2016**, *304*, 594–601. [[CrossRef](#)]
37. Chang, F.; Xie, Y.; Li, C.; Chen, J.; Luo, J.; Hu, X.; Shen, J. A facile modification of g- $C_3N_4$  with enhanced photocatalytic activity for degradation of methylene blue. *Appl. Surf. Sci.* **2013**, *280*, 967–974. [[CrossRef](#)]
38. Thomas, A.; Fischer, A.; Goettmann, F.; Antonietti, M.; Mueller, J.O.; Schloegl, R.; Carlsson, J.M. Cheminform abstract: Graphitic carbon nitride materials: Variation of structure and morphology and their use as metal-free catalysts. *J. Mater. Chem.* **2008**, *40*, 4893–4908. [[CrossRef](#)]
39. Thomas, M.; Ghosh, S.K.; George, K.C. Characterisation of nanostructured silver orthophosphate. *Mater. Lett.* **2002**, *56*, 386–392. [[CrossRef](#)]
40. Pan, C.; Xu, J.; Wang, Y.; Li, D.; Zhu, Y. Dramatic activity of  $C_3N_4/BiPO_4$  photocatalyst with core/shell structure formed by self-assembly. *Adv. Funct. Mater.* **2012**, *22*, 1518–1524. [[CrossRef](#)]
41. Li, X.F.; Zhang, J.; Shen, L.H.; Ma, Y.M.; Lei, W.W.; Cui, Q.L.; Zou, G.T. Preparation and characterization of graphitic carbon nitride through pyrolysis of melamine. *Appl. Phys. A Mater.* **2009**, *94*, 387–392. [[CrossRef](#)]
42. Cui, Y.; Ding, Z.; Fu, X.; Wang, X. Construction of conjugated carbon nitride nanoarchitectures in solution at low temperatures for photoredox catalysis. *Angew. Chem.* **2012**, *51*, 11814–11818. [[CrossRef](#)] [[PubMed](#)]
43. Bu, Y.; Chen, Z. Role of polyaniline on the photocatalytic degradation and stability performance of the polyaniline/silver/silver phosphate composite under visible light. *ACS Appl. Mater. Interfaces* **2014**, *6*, 17589–17598. [[CrossRef](#)] [[PubMed](#)]
44. Yan, S.C.; Li, Z.S.; Zou, Z.G. Photodegradation performance of g- $C_3N_4$  fabricated by directly heating melamine. *Langmuir* **2009**, *25*, 10397–10401. [[CrossRef](#)] [[PubMed](#)]
45. Michael, I.; Achilleos, A.; Lambropoulou, D.; Torrens, V.O.; Pérez, S.; Petrović, M.; Barceló, D.; Fatta-Kassinos, D. Proposed transformation pathway and evolution profile of diclofenac and ibuprofen transformation products during (sono)photocatalysis. *Appl. Catal. B Environ.* **2014**, *147*, 1015–1027. [[CrossRef](#)]
46. Chong, S.; Zhang, G.; Wei, Z.; Zhang, N.; Huang, T.; Liu, Y. Sonocatalytic degradation of diclofenac with feceox particles in water. *Ultrason. Sonochem.* **2017**, *34*, 418–425. [[CrossRef](#)] [[PubMed](#)]

47. Cheng, X.; Liu, H.; Chen, Q.; Li, J.; Wang, P. Preparation and characterization of palladium nano-crystallite decorated TiO<sub>2</sub> nano-tubes photoelectrode and its enhanced photocatalytic efficiency for degradation of diclofenac. *J. Hazard. Mater.* **2013**, *254–255*, 141–148. [[CrossRef](#)] [[PubMed](#)]
48. Shan, C.; Zhang, G.; Nan, Z.; Liu, Y.; Huang, T.; Chang, H. Diclofenac degradation in water by FeCeO<sub>x</sub> catalyzed H<sub>2</sub>O<sub>2</sub>: Influencing factors, mechanism and pathways. *J. Hazard. Mater.* **2017**, *334*, 150–159.
49. Liu, S.; Zhao, X.; Zeng, H.; Wang, Y.; Qiao, M.; Guan, W. Enhancement of photoelectrocatalytic degradation of diclofenac with persulfate activated by Cu cathode. *Chem. Eng. J.* **2017**, *320*, 168–177. [[CrossRef](#)]
50. Baukhatem, H.; Khalaf, H.; Djouadi, L.; Marin, Z.; Navarro, R.M.; Santaballa, J.A.; Canle, M. Diclofenac degradation using mont-La(6%)-Cu<sub>0.6</sub>Cd<sub>0.4</sub>S as photocatalyst under NUV-Vis irradiation. Operational parameters, kinetics and mechanism. *J. Environ. Chem. Eng.* **2017**, *180*, 5636–5644. [[CrossRef](#)]
51. Martínez, C.; Canle, L.M.; Fernández, M.I.; Santaballa, J.A.; Faria, J. Aqueous degradation of diclofenac by heterogeneous photocatalysis using nanostructured materials. *Appl. Catal. B Environ.* **2011**, *107*, 110–118. [[CrossRef](#)]
52. Aguera, A.; Perez Estrada, L.A.; Ferrer, I.; Thurman, E.M.; Malato, S.; Fernandez-Alba, A.R. Application of time-of-flight mass spectrometry to the analysis of phototransformation products of diclofenac in water under natural sunlight. *J. Mass Spectrom.* **2005**, *40*, 908–915. [[CrossRef](#)] [[PubMed](#)]
53. Bi, Y.; Ouyang, S.; Cao, J.; Ye, J. Facile synthesis of rhombic dodecahedral AgX/Ag<sub>3</sub>PO<sub>4</sub> (X = Cl, Br, I) heterocrystals with enhanced photocatalytic properties and stabilities. *Phys. Chem. Chem. Phys.* **2011**, *13*, 10071–10075. [[CrossRef](#)] [[PubMed](#)]
54. Zhou, L.; Zhang, W.; Chen, L.; Deng, H. Z-scheme mechanism of photogenerated carriers for hybrid photocatalyst Ag<sub>3</sub>PO<sub>4</sub>/g-C<sub>3</sub>N<sub>4</sub> in degradation of sulfamethoxazole. *J. Colloid Interface Sci.* **2017**, *487*, 410–417. [[CrossRef](#)] [[PubMed](#)]
55. Miyauchi, M. Photocatalysis and photoinduced hydrophilicity of WO<sub>3</sub> thin films with underlying Pt nanoparticles. *Phys. Chem. Chem. Phys.* **2008**, *10*, 6258–6265. [[CrossRef](#)] [[PubMed](#)]
56. Yan, H.J.; Chen, Y.; Xu, S.M. Synthesis of graphitic carbon nitride by directly heating sulfuric acid treated melamine for enhanced photocatalytic H<sub>2</sub> production from water under visible light. *Int. J. Hydrogen Energy* **2012**, *37*, 125–133. [[CrossRef](#)]



© 2018 by the authors. Licensee MDPI, Basel, Switzerland. This article is an open access article distributed under the terms and conditions of the Creative Commons Attribution (CC BY) license (<http://creativecommons.org/licenses/by/4.0/>).